



Cite this: DOI: 10.1039/d5dt01436k

Dual-confined carbon dots in B₂O₃ for orange-yellow room-temperature phosphorescence†

Juan Dong,^a Zengsheng Guo,^a Jin-Shuang Guo,^c Jingtian Xue,^a Yilei Wang,^a Yiqiang Sun,^a ^a Guang-Ning Liu ^{*a} and Cuncheng Li ^{*a,b}

Room-temperature phosphorescent (RTP) carbon dot (CDs) materials have attracted significant interest due to their excellent biocompatibility, large Stokes shift, and potential for anti-counterfeiting applications. However, the preparation of long-wavelength-emitting phosphorescent materials based on CDs remains a challenge, as most RTP CDs exhibit blue and green emissions. Here, we designed a double confinement strategy to obtain orange-yellow RTP CDs composites (CDs@B₂O₃) via hydrothermal treatment and calcination. After calcination, the phosphorescence emission of the composite material underwent a significant red shift (546 to 582 nm). Simultaneously, under 468 nm excitation, CDs@B₂O₃-350 showed both fluorescence emission centred at 521 nm and phosphorescence emission centred at 582 and 627 nm. Structural and chemical characterizations, as well as optical studies, revealed that the CDs@B₂O₃ composite material features a highly rigid network with electron traps and stable covalent bonds, which generate multiple confinement effects. This material demonstrates great potential for application in the field of multi-level information encryption.

Received 18th June 2025,
Accepted 17th July 2025

DOI: 10.1039/d5dt01436k

rsc.li/dalton

1. Introduction

Room-temperature phosphorescent (RTP) materials are widely used in fields such as information anti-counterfeiting, optical sensing, bioimaging, light-emitting diodes, and latent fingerprint detection, due to their large Stokes shift and long-lived afterglow. Existing RTP phosphorescent materials typically rely on rare-earth elements or purely organic compounds.^{1–8} However, these materials suffer from issues such as short afterglow lifetimes, low stability, and non-negligible toxicity.^{9,10} Carbon Dots (CDs) have emerged as promising metal-free alternatives due to their low toxicity, facile synthesis, and abundant surface functional groups. However, the phosphorescence emission of CDs is primarily associated with the radiative transition of triplet excitons.^{11–13} Given that triplet excitons are related to spin-forbidden transitions, they are easily dissipated by molecular thermal vibrations and quenched by triplet-state oxygen at room temperature and

higher temperatures, making it difficult to achieve room-temperature phosphorescence.¹⁴

Current research indicates that the phosphorescence characteristics of CDs can be realized through two main strategies: heteroatom doping and matrix embedding. Among these, the matrix-assisted approach has garnered substantial attention in recent years due to its universality. Suitable matrix materials include organic matrices (such as polyvinyl alcohol, urea/biuret, *etc.*) and inorganic matrices (such as silica, inorganic salts, *etc.*).^{15–18} When CDs are confined within rigid matrices, the restrictive effects of the matrix-through hydrogen bonding, covalent bonding, or spatial constraints-not only stabilize triplet excitons but also effectively promote the emission of RTP. However, the resulting CDs@matrix composite materials primarily emit green phosphorescence, which severely limits their practical application potential.^{19–22} For instance, Zhuang *et al.* propose a universal “CDs-in-YOHF” strategy to generate long-wavelength RTP by confining various CDs in the YOHF matrix.²³ Zheng *et al.* report a rational strategy of multiple wavelength excitation and time-dependent dynamic RTP color by confining silane-functionalized CDs in a silica matrix (Si-CDs@SiO₂). The Si-CDs@SiO₂ possesses unique green-light-excitation and a change in phosphorescence color from yellow to green.²⁴ Therefore, the development of long-wavelength, highly efficient phosphorescent materials based on CDs remains an urgent scientific challenge that needs to be addressed.^{25–30}

In this work, we have successfully engineered a dual-constraint strategy to obtain CDs@B₂O₃ via a hydrothermal treat-

^aSchool of Chemistry and Chemical Engineering, University of Jinan, Jinan 250022, P. R. China. E-mail: chm_liugn@ujn.edu.cn, chm_liicc@ujn.edu.cn

^bCollaborative Innovation Center of Yellow River Basin Pharmaceutical Green Manufacturing and Engineering Equipment, University of Jinan, Jinan 250022, P. R. China

^cCharacteristic Laboratory of Forensic Science in Universities of Shandong Province, Shandong University of Political Science and Law, Jinan, Shandong, 250014, P. R. China

† Electronic supplementary information (ESI) available. See DOI: <https://doi.org/10.1039/d5dt01436k>

ment followed by calcination. After calcination, the degree of carbonization of the CDs increased, and the optimal phosphorescence emission wavelength of the CDs@B₂O₃ composite material also undergoes a red shift from 546 nm to 582 nm. Simultaneously, under 468 nm excitation, CDs@B₂O₃-350 showed both fluorescence emission centred at 521 nm and phosphorescence emission centred at 582 and 627 nm. This study demonstrates that the excellent RTP performance is attributed to the synergistic effect of the rigid network and the formed covalent bonds, highlighting its potential application in optical anti-counterfeiting.

2. Experimental

2.1 Chemicals and materials

Boric acid was obtained from Tianjin Zhiyuan Chemical Reagent Co., Ltd. 1,3,6-Trinitroacridine was prepared by condensation reflux of pyrene with nitric acid. Sodium hydroxide was obtained from Tianjin Zhiyuan Chemical Reagent Co., Ltd. All reagents were used as received without further purification. Deionized water was used throughout the experiments.

2.2 Preparation of CDs@B₂O₃ composite materials

Specifically, 30 mg 1,3,6-trinitropyrene was dissolved in 10 mL of 0.2 mol L⁻¹ sodium hydroxide aqueous solution under sonication until complete dissolution. Subsequently, boric acid (0.6183 g) was added to the mixture, followed by an additional 30 minutes of sonication. The resulting mixture was then transferred into a 25 mL Teflon-lined autoclave and heated at 180 °C for 12 h. After cooling to room temperature, the reaction mixture was filtered through a 0.22 μm nylon membrane to remove precipitates. The filtrate was then freeze-dried to obtain CDs@B₂O₃. The product was ground into a powder and heated in air at a rate of 5 °C min⁻¹ to different calcination temperatures (250, 350 and 450 °C) and maintained at each temperature for 2 h to obtain the CDs@B₂O₃-X (X = 250, 350, and 450 °C) samples.

2.3 Characterization

The morphology and structural characteristics of the synthesized samples were meticulously investigated employing various analytical techniques. Transmission electron microscopy (TEM, JEOL JEM 2100F) was employed to elucidate the morphologies and structures of the samples. A Cu Kα radiation source (λ = 1.5406 Å) was employed for powder X-ray diffraction (XRD) using a Bruker D8 Focus 2000 X-ray diffractometer. X-ray photoelectron spectroscopy (XPS) spectra were acquired using an ESCALAB 250 spectrometer. UV-Vis absorption spectra were obtained from samples using a Shimadzu UV-2550 spectrophotometer. The fluorescence and phosphorescence spectra of the samples were collected using a steady-state and transient fluorescence spectrometer, model FLS1000, produced by Edinburgh Instruments, UK. The fluorescence spectra were measured using a xenon lamp as the light source. The phosphorescence spectra and lifetime decay curves were

tested with a microsecond lamp as the light source. The phosphorescence spectra at different temperatures were measured using the OXF XRD cryogenic accessory.

3. Results and discussion

As shown in Fig. 1, 1,3,6-trinitropyrene and boric acid were used as raw materials for hydrothermal synthesis at 180 °C for 12 h. Subsequently, the product was filtered and freeze-dried to obtain a yellow-green fluorescent powder (CDs@HBO₂-180).³¹ The final CDs@B₂O₃-X (X = 250, 350, and 450) were obtained after calcination. Firstly, the morphology and microstructure of the material are investigated by transmission electron microscopy (TEM).³² Fig. 2a and Fig. S1, S2, ESI† shows the CDs exhibit a spherical shape and are uniformly distributed within the B₂O₃ matrix. The rise of calcination temperature from 250 °C to 450 °C results in the decrease of average CDs size from 3.37 nm to 1.69 nm.³³ The inserted high-resolution transmission electron microscopy (HRTEM) images in Fig. 2b and Fig. S3, ESI† show clear lattice fringes of the CDs@B₂O₃-250, CDs@B₂O₃-350 and CDs@B₂O₃-450, with a lattice spacing of 0.21 nm, corresponding to the (100) crystal plane of graphite.³⁴

Furthermore, the elemental mapping images demonstrated the homogeneous dispersion of B, O, N and C atoms, further confirming the successful fabrication of the CDs@B₂O₃ (Fig. S4, ESI†). In the XRD pattern of CDs@B₂O₃-350, the diffraction peaks of B₂O₃ appeared at 2θ = 14.70°, 27.74°, and 41.58° (JCPDS no. 06-0297), indicating the presence of B₂O₃ structure in the composite (Fig. 2c). At 180 °C, boric acid cannot be converted into boric oxide but instead forms HBO₂ (Fig. S5, ESI†).³⁵ Additionally, the CDs@B₂O₃-350 exhibited a significantly high Raman intensity ratio (I_G/I_D = 1.51), indicating a high degree of graphitization (Fig. S6, ESI†).³⁶ To investigate the chemical interactions between CDs and B₂O₃, Fourier

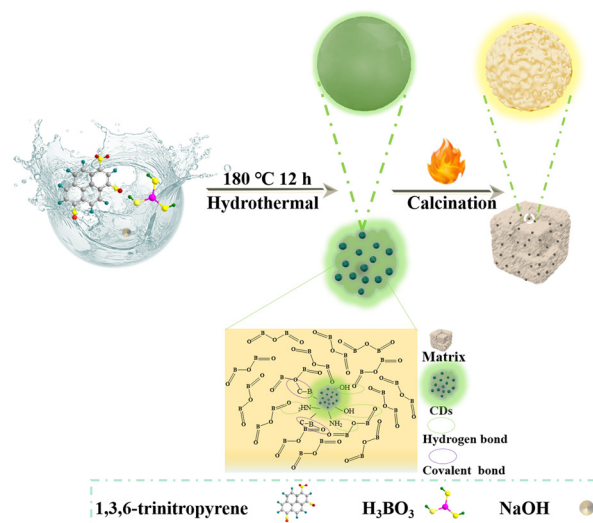


Fig. 1 Schematic illustration for the synthesis of CDs@B₂O₃.

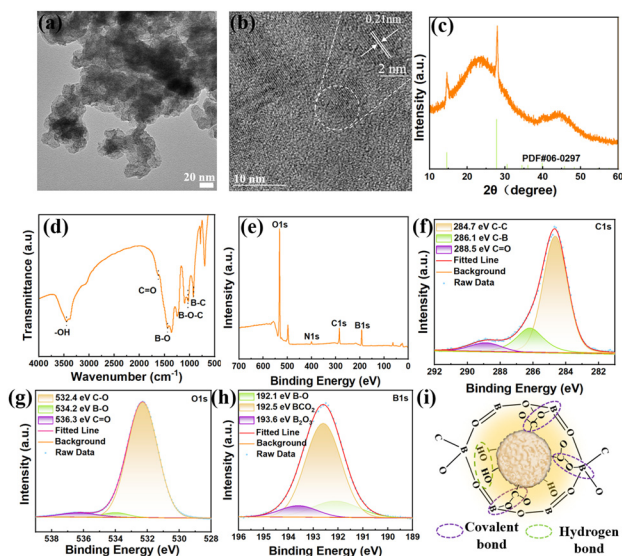


Fig. 2 (a) TEM and (b) HRTEM (inset) images of CDs@B₂O₃-350. (c) XRD patterns of CDs@B₂O₃-350. (d) FTIR spectrum of CDs@B₂O₃-350. (e) XPS survey spectrum of CDs@B₂O₃-350. (f) High-resolution C1s XPS spectrum of CDs@B₂O₃-350. (g) High-resolution O1s XPS spectrum of CDs@B₂O₃-350. (h) High resolution B1s XPS spectrum of CDs@B₂O₃-350. (i) Schematic of the proposed structure of CDs@B₂O₃ composite material.

transform infrared (FT-IR) spectroscopy were performed on CDs@B₂O₃-350 material. As displayed in Fig. 2d, the characteristic absorption bands at 3420 and 1650 cm⁻¹ were assigned to the stretching vibration of -OH and C=O of CDs. The absorption bands at about 1450 and 1196 cm⁻¹ were attributed to the stretching vibrations of B-O and the asymmetrically stretched oxygen atom connecting the trigonal boron atoms of BA, simultaneously. Further, the appearance of absorption band at 928 cm⁻¹ of B-C bond, indicating the formation of B₂O₃ during the calcination process.³⁷ Compared with the IR spectrum of CDs@B₂O₃-350, the FT-IR spectrum of CDs@HBO₂-180 shows characteristic peaks at 1400–1500 and 1197 cm⁻¹, which are assigned to the stretching vibration of B-O and the asymmetric stretching vibration of B-O in the B-O-B bond connecting the trigonal and tetrahedral B atomic units, respectively. Additionally, the absorption peak at 655 cm⁻¹ is derived from the bending vibration of B-O-H. These results indicate that the B₂O₃ matrix is formed through the gradual dehydration of BA during the heating process (Fig. S5, ESI†).³⁸ In order to further validate the analysis results of FT-IR, X-ray photoelectron spectroscopy (XPS) was used to study the main components of the CDs@B₂O₃-350 composite. As shown in Fig. 2e, the XPS spectrum of CDs@B₂O₃-350 revealed four peaks at 532.1, 400.08, 285.2 and 192.1 eV, corresponding to O 1s, N 1s, C 1s, and B 1s, respectively. In the high-resolution C1s XPS spectra (Fig. 2f), three fitted peaks at 284.7 eV, 286.1 eV, and 288.5 eV were observed, corresponding to C-C, C-B and C=O bonds, respectively. In the high-resolution O 1s spectra, three binding energies at 532.4 eV, 534.2 eV, and 536.3 eV were detected, corresponding to C-O, B-O, and C=O

bonds, respectively (Fig. 2g). Similarly, in the high-resolution B 1s spectra, three binding energies at 192.5, 192.1, and 193.6 eV were observed, corresponding to BCO₂, B-O, and B₂O₃ bonds, respectively (Fig. 2h). Furthermore, in the high-resolution N 1s spectra, two peaks at 399.8 eV and 401.7 eV were observed, corresponding to pyridine-like and graphite-like structures, respectively (Fig. S7, ESI†). The presence of B-C in CDs@B₂O₃-250 and CDs@B₂O₃-450 is also evident (Fig. S8, ESI†). FT-IR and XPS spectra consistently demonstrate that CDs are covalently bonded into the B₂O₃ matrix.^{39–41} These characterization results clearly indicate the formation of robust chemical linkages between CDs and the boron oxide framework. As shown in Fig. 2i, the structural and potential bonding configuration between CDs and B₂O₃ indicates that for CDs@B₂O₃-350, the long-wavelength RTP emission arises from the dual-confinement effect of these strong covalent bonds and the highly rigid structure. This unique dual-confinement mechanism effectively suppresses nonradiative transitions of triplet excitons in CDs and promotes intersystem crossing to generate more triplet excitons.^{42,43}

To investigate the factors influencing the phosphorescence emission, a comprehensive analysis of their optical properties was conducted. As shown in Fig. 3a, CDs@B₂O₃-350 exhibits bright orange-yellow RTP under UV excitation, with a naked-eye-visible afterglow lasting up to 14 s. The UV-vis absorption spectrum of CDs@B₂O₃-350 features two characteristic absorption peaks at 250 nm and 375 nm, corresponding to the π-π* transition of the C-C bond and the n-π* transition of the C=O group, respectively. Notably, for CDs@B₂O₃-350, an obvious broad absorption band appears at 390–500 nm, which is attributed to the nitrogen atoms with lone pair electrons facilitating the formation of the n-π* electronic configuration,

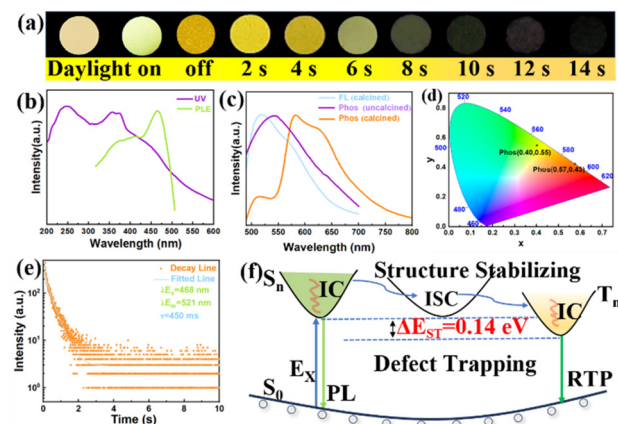


Fig. 3 (a) Photographs of CDs@B₂O₃-350 powder taken at different time intervals after the cessation of 365 nm UV irradiation. (b) Absorption and photoluminescence excitation spectra (Ex = 468 nm) of CDs@B₂O₃-350. (c) Normalized fluorescence emission (blue) and phosphorescence emission spectra of CDs@B₂O₃-350 (orange) and CDs@HBO₂-180 (purple). (d) CIE coordinates of the phosphorescence emission of CDs@B₂O₃-350 and CDs@HBO₂-180. (e) Time-resolved phosphorescence decay and fitting curve of CDs@B₂O₃-350. (f) Energy level diagram of CDs@B₂O₃.

thereby resulting in a red-shift in the absorption spectrum.⁴⁴ The excitation spectrum covers a broad range from 250 to 500 nm, with the optimal excitation wavelength at 468 nm (Fig. 3b). The photoluminescence properties, including fluorescence and phosphorescence spectra, were further investigated through normalization. Under 468 nm excitation, CDs@B₂O₃-350 showed both fluorescence emission centred at 521 nm and phosphorescence emission centred at 582 and 627 nm. Also, the exceptionally long wavelength emission surpasses all previously reported phosphorescence emission wavelengths of other carbon dots (Table S1, ESI†). At the same time, the phosphorescence emission center of the uncalcined composite is located at 546 nm.

The distinct shoulder peak observed at 627 nm can be attributed to a synergistic interplay of the following mechanisms: as a large-conjugated aromatic chromophore, 1,3,6-trinitropyrene establishes an extended π -electron conjugated platform through its pyrene-fused ring architecture, significantly enhancing electron delocalization effects. Concurrently, CDs embedded within the boron oxide matrix exhibit polydisperse aggregated states. The resulting energy-level coupling between variably aggregated CDs and the 1,3,6-trinitropyrene-boric acid composite system gives rise to a characteristic shoulder peak in the long-wavelength region of the phosphorescence spectrum.⁴⁵ Notably, the phosphorescence emission centres show a significant red shift compared with the uncalcined sample of CDs@B₂O₃ (centred at 546 nm). The significant red shift in the phosphorescence spectrum after calcination occurs because the nitro groups (-NO₂) of 1,3,6-pyrene are strong electron-withdrawing groups. These groups alter the electronic distribution of the polycyclic aromatic hydrocarbons through a conjugation effect. Calcination promotes the synergistic cross-linking of the nitro groups with boric acid, forming a more stable rigid network. This further suppresses molecular vibrations and rotations, while also modulating the excited-state energy levels (Fig. 3c).⁴⁶ Furthermore, the Commission Internationale de l'Eclairage (CIE) coordinates are consistent with the red-shifted phosphorescence emission phenomena (Fig. 3d). To gain insights into the long lifetime properties of CDs@B₂O₃-350, we employed phosphorescence decay spectroscopy to analyze the exciton dynamics. As shown in Fig. 3e, the RTP properties of CDs@B₂O₃-350 were further characterized through the analysis of phosphorescence decay curves. By fitting a triexponential function to this curve, according to the following equation:

$$\tau_{\text{avg}} = \sum \alpha_i \tau_i^2 / \sum \alpha_i \tau_i$$

CDs@B₂O₃-350 was found to exhibit an average lifetime of 450 ms. To verify that the afterglow is RTP, the temperature-dependent phosphorescence spectra of CDs@B₂O₃-350 under 468 nm excitation were tested, as shown in Fig. S9, ESI†. As the temperature increases from 77 K to 300 K, the afterglow intensity of CDs@B₂O₃-350 gradually weakens, confirming that the afterglow of CDs@B₂O₃-350 is RTP rather than thermally activated delayed fluorescence (TADF). Additionally, the fluo-

rescence and phosphorescence spectra were recorded at low temperatures to estimate ΔE_{ST} (Fig. S10, ESI†). The ΔE_{ST} between the lowest triplet state (T₁) and the lowest singlet state (S₁) was estimated to be 0.14 eV (S₁ = 2.27 eV and T₁ = 2.13 eV). The relatively large ΔE_{ST} exceeds the typical threshold for efficient TADF (≤ 0.1 eV), further supporting the conclusion that the afterglow originates from RTP rather than TADF.⁴⁷

During the preparation of CDs@B₂O₃, the calcination temperature plays a crucial role in determining its phosphorescence properties. By evaluating the phosphorescence spectra and attenuation curves of samples calcined at different temperatures (Fig. S11, S12 and Table S2, ESI†). It was observed that the phosphorescence intensity and lifetime of CDs@B₂O₃-350 gradually increase as the calcination temperature rises from 250 to 350 °C. This improvement can be attributed to the enhanced rigidity provided by the compact short-range ordered structure within the amorphous B–O–C network.^{48,49} However, further increasing the calcination temperature to 450 °C leads to a reduction in both phosphorescence intensity and lifetime. Additionally, the higher calcination temperature (350 to 450 °C) induces a blue shift in the phosphorescence emission peak (from 582 nm to 530 nm), which is closely associated with the decreased size of CDs (Fig. S2 and S11, ESI†) and the declining carbon content (Table S3, ESI†). Notably, CDs@B₂O₃-350 exhibits the strongest and longest-lived phosphorescence after the removal of 365 nm UV excitation, confirming its superior performance (Fig. S13, ESI†). As shown in Fig. S14, ESI† further XRD analysis revealed that the diffraction peaks for CDs@B₂O₃-350 are sharper than those for both CDs@B₂O₃-250 and CDs@B₂O₃-450, which indicates that CDs@B₂O₃-350 has an optimized crystalline state.^{50–52}

To correlate defect density with phosphorescence efficiency, electron paramagnetic resonance (EPR) spectra of CDs@B₂O₃-250, CDs@B₂O₃-350 and CDs@B₂O₃-450 were systematically compared (Fig. S15, ESI†). The EPR signal intensity initially increases but then decreases with rising calcination temperature. At the optimal calcination temperature of 350 °C, oxygen vacancies are generated on the CDs surface due to the dissociation of oxygen atoms in the B₂O₃ matrix, forming covalent bonds and increasing defect density. However, at 450 °C, the consumption of carbon dots reduces the number of luminescent centres, while the B₂O₃ matrix undergoes defect annihilation, leading to a significant decrease in EPR signal intensity.^{53–56} Based on these findings, we propose a mechanism for the enhanced afterglow and tunable luminescence of CDs@B₂O₃-350 (Fig. 3f). Structural analyses confirm the formation of B–C and B–O covalent bonds on the CDs surface. We hypothesize the RTP mechanism as follows: under UV light excitation, electrons in the S₀ state are promoted to the excited state. The resulting excitons can either undergo internal conversion, emitting fluorescence as they decay radiatively from S₁ to S₀ or proceed *via* intersystem crossing (ISC) to the T₁ state, generating phosphorescence. Oxygen vacancies and other defect trap stabilize singlet excitons, enabling their transition to T₁ *via* phosphorescence emission before returning to the ground state (S₀). Thus, the B–O–C network not only

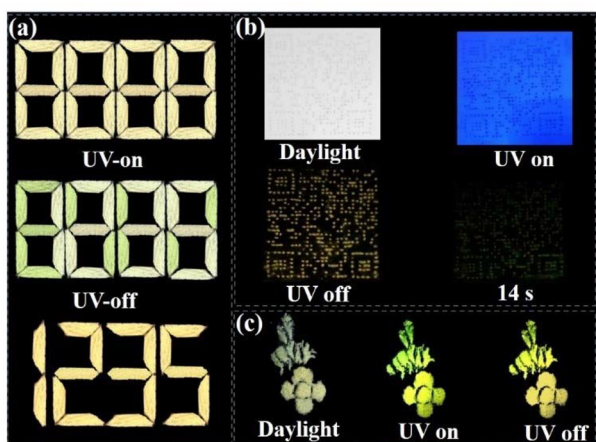


Fig. 4 (a) Demonstration of information encryption application. The encrypted numerical term “1235” painted with $\text{CDs@B}_2\text{O}_3\text{-350}$ and the remaining part painted with $\text{CDs@HBO}_2\text{-180}$. (b) QR code information protection application of $\text{CDs@B}_2\text{O}_3\text{-350}$. (c) Phosphorescence photographs of bees painted with $\text{CDs@HBO}_2\text{-180}$ and flowers painted with $\text{CDs@B}_2\text{O}_3\text{-350}$.

protect triplet excitons, but also traps free electrons, thereby slowing the ISC process.^{57,58}

The outstanding RTP performance of $\text{CDs@B}_2\text{O}_3$ demonstrates great potential for anti-counterfeiting and encryption technologies. As shown in Fig. 4a, the numerical term “8888” is divided into two parts: the encrypted numerical term “1235” and the remaining part. Under irradiation by a 365 nm UV lamp, the green fluorescent number “8888” becomes visible. When the UV lamp is turned off, the final encrypted term “1235” appears. The application of $\text{CDs@B}_2\text{O}_3$ was further explored for dual-mode security protection.^{59–61} As shown in Fig. 4b, a QR (quick response) code was fabricated using $\text{CDs@B}_2\text{O}_3$ paint. Under 365 nm UV irradiation, the QR code was encrypted under intense bright blue light, making it unrecognizable when scanned with a smartphone. After the UV light was turned off, the short-lived fluorescence of the paper disappeared, revealing a very clear QR code.⁶² The pattern consists of flowers and bees. Under UV irradiation, bees exhibits a green color, while after the UV light is turned off, it displays a yellow color. Under UV light irradiation, the flower exhibits a yellow-green color, while after the UV light is turned off, it displays an orange-yellow color. The color change of the pattern highlights the promising prospects of the $\text{CDs@B}_2\text{O}_3$ material in anti-counterfeiting applications (Fig. 4c).⁶³

Conclusions

In summary, we successfully designed a dual-constraint strategy to obtain $\text{CDs@B}_2\text{O}_3$ through hydrothermal treatment and calcination. After calcination, the phosphorescence emission of the composite material underwent a significant red shift. Simultaneously, under 468 nm excitation, $\text{CDs@B}_2\text{O}_3\text{-350}$

showed both fluorescence emission centred at 521 nm and phosphorescence emission centred at 582 and 627 nm. The presence of B–C covalent bonds effectively suppresses the non-radiative transitions of the triplet states of CDs and promotes intersystem crossing. This, in combination with the stable and rigid structure of boron oxide, synergistically generates long-wavelength RTP emission. Based on the excellent afterglow emission characteristics of the long-wavelength RTP emission, these materials hold great potential for multi-level information encryption.

Author contributions

Juan Dong: Investigation, methodology, writing – original draft. Zengsheng Guo: Methodology, validation. Jin-Shuang Guo: Validation. Jingtian Xue: Investigation, Yilei Wang: Methodology. Yiqiang Sun: Methodology, validation. Guang-Ning Liu: Validation, writing – review & editing. Cuncheng Li: Conceptualization, supervision, writing – review & editing, funding acquisition.

Conflicts of interest

There are no conflicts to declare.

Data availability

The data that support the findings of this study are available on request from the corresponding author upon reasonable request.

Acknowledgements

This study is provided by National Natural Science Foundation of China (Grant no. 52171179), National Natural Science Foundation of Shandong province (Grant no. ZR2024MB006), Collaborative Innovation Center of Yellow River Basin Pharmaceutical Green Manufacturing and Engineering Equipment, Jinan City University Integration Development Strategy Project (Grant no. JNSX2023021).

References

- Z. Q. Zhao, L. Tan, T. B. Lv, J. J. Zhang, K. M. Liao, H. Y. Wang, Z. L. Zeng, S. G. Deng and G. P. Dai, *ACS Appl. Nano Mater.*, 2024, 7, 13736–13744.
- W. J. Cao, W. J. Zhang, L. Dong, Z. Ma, J. S. Xu, X. L. Gu and Z. P. Chen, *Exploration*, 2023, 3, 20220169.
- W. He, X. Sun and X. Cao, *ACS Chem. Eng.*, 2021, 9, 4477–4486.

- 4 J. R. Gao, K. S. Zhang, S. Y. Huang, L. Tang, L. Chen, R. X. He, M. Li and W. Shen, *ACS Appl. Nano Mater.*, 2024, **7**, 6109–6119.
- 5 Y. Q. Sun, S. T. Liu, L. Y. Sun, S. S. Wu, G. Q. Hu, X. L. Pang, A. T. Smith, C. F. Hu, S. S. Zeng, W. X. Wang, Y. L. Liu and M. T. Zheng, *Nat. Commun.*, 2020, **11**, 5591.
- 6 P. Liu, C. Liu, J. C. Chen and B. Wang, *Nano Lett.*, 2025, **25**, 434–442.
- 7 T. Zhang, J. P. Zhou, H. M. Li, J. Ma, X. Wang, H. Q. Shi, H. M. Niu, Y. S. Liu, F. S. Zhang and Y. Z. Guo, *Green Chem.*, 2023, **25**, 1406–1416.
- 8 Z. H. Yan, Z. Y. Feng, S. Zhou and X. M. Yang, *Chem. Eng. J.*, 2024, **494**, 152835.
- 9 X. P. Wang, S. X. Xie, L. L. Tao and M. T. OuYang, *J. Mater. Chem. C*, 2024, **12**, 5849.
- 10 Y. N. Jie, Y. Gao, D. Wang, F. C. Li, R. F. Chen, Y. Q. Feng, W. Q. Li and J. W. Fang, *New J. Chem.*, 2023, **47**, 16659.
- 11 X. Wei, X. Y. Wang, Y. Fu, X. Y. Zhang and F. Y. Yan, *Microchim. Acta*, 2024, **191**, 355.
- 12 W. B. You, W. T. Zou, S. Y. Jiang, J. H. Zhang, Y. G. Ge, G. Lu, D. W. Bahnemann and J. H. Pan, *Carbon Neutralization*, 2024, **3**, 245–284.
- 13 Z. Z. Li, S. Cao, Y. Y. Zheng, L. Q. Song, H. Q. Zhang and Y. L. Zhao, *Adv. Funct. Mater.*, 2024, **34**, 2306956.
- 14 L. Chen, S. B. Zhao, Y. Wang, S. P. Yu, Y. Z. Yang and X. G. Liu, *Sens. Actuators, B*, 2023, **390**, 133946.
- 15 C. Y. Zhang, J. D. Guo, P. W. Kong, S. Q. Zhou, M. Y. Wu, J. S. Pen, X. B. Li, C. X. Chen and H. W. Ma, *Mater. Today Chem.*, 2025, **43**, 102508.
- 16 K. Jiang, S. Z. Hu, Y. C. Wang, Z. J. Li and H. W. Lin, *Small*, 2020, **16**, 2001909.
- 17 P. Liang, Y. Zheng and X. Zhang, *Small*, 2022, **13**, 5127–5136.
- 18 D. Lu, K. Lu, H. T. Wen, Z. Wei, A. Bianco, G. G. Wang and H. Y. Zhang, *Small*, 2023, **19**, 2207046.
- 19 Z. S. Guo, X. D. Yang, B. Xu, G. N. Liu, Y. Q. Sun and C. C. Li, *ACS Appl. Nano Mater.*, 2023, **6**, 23548–23556.
- 20 Y. Fu, G. Y. Gao and J. F. Zhi, *J. Mater. Chem. B*, 2019, **7**, 1494–1502.
- 21 H. Hu, X. Zhao and X. Mao, *ACS Appl. Nano Mater.*, 2024, **7**, 22525–22533.
- 22 J. Chen, J. Tan and P. Liang, *Small*, 2024, **16**, 2306323.
- 23 P. Liang, Y. H. Zheng, X. C. Zhang, X. K. Xu, X. F. Yang, H. P. Wei, H. H. Lin, C. F. Hu, X. J. Zhang, B. F. Lei, Y. L. Liu and J. L. Zhuang, *Nano Lett.*, 2022, **22**, 5127–5136.
- 24 J. Y. Chen, J. Q. Tan, P. Liang, C. J. Wu, Z. L. Hou, K. Y. Shen, B. F. Lei, C. F. Hu, X. J. Zhang, J. L. Zhuang, L. Y. Sun, Y. L. Liu and M. T. Zheng, *Small*, 2024, **20**, 2306323.
- 25 Z. S. Guo, C. C. Wang, F. Z. Qi, J. Dong, Y. L. Wang, Y. Q. Sun and C. C. Li, *Adv. Funct. Mater.*, 2025, **35**, 2414178.
- 26 Z. Z. Ding, C. L. Shen, J. F. Han, G. S. Zheng, C. Ni, R. W. Song, K. K. Liu, J. H. Zang, L. Dong, Q. Lou and C. X. Shan, *Small*, 2022, **19**, 2205916.
- 27 X. Huang, M. Q. Shi, H. Q. Zhai, Y. X. Zhang, Y. L. Zhang and Y. X. Zhao, *Polym. Chem.*, 2023, **14**, 268–276.
- 28 Q. Feng, Z. G. Xie and M. Zheng, *Sens. Actuators, B*, 2022, **351**, 130976.
- 29 W. G. Chen, Y. F. Zhuang, Y. Wang, Z. J. Chen, Y. F. Lv, S. Fu and Y. Chen, *Chem. Eng. J.*, 2025, **503**, 158381.
- 30 Y. F. Ding, X. L. Wang, M. Tang and H. B. Qiu, *Adv. Sci.*, 2022, **9**, 2103833.
- 31 S. Fu, B. J. Tang, Z. M. Wang, G. B. An, M. W. Zhang, K. Wang, W. H. Liu, H. Z. Guo, B. H. Zhang and L. Wang, *Chem. Eng. J.*, 2024, **500**, 157207.
- 32 W. D. Hou, H. Z. Guo, K. Wang, T. Hao, J. Y. Zhang, M. H. Wu and L. Wang, *Mater. Today*, 2025, **84**, 1–9.
- 33 T. Zhang, M. Y. Wang, L. L. Liu, Z. J. Li and H. Bi, *Adv. Funct. Mater.*, 2024, **34**, 2406672.
- 34 S. Q. Cui, B. W. Wang, Y. W. Zan, Z. Y. Shen, S. W. Wang, X. L. Yan, Y. Li and L. G. Chen, *Chem. Eng. J.*, 2022, **431**, 133373.
- 35 Z. S. Zhou, K. F. Jiang, N. A. D. Chen, Z. F. Xie, B. F. Lei, J. L. Zhuang, Y. L. Liu and C. F. Hu, *Mater. Lett.*, 2020, **276**, 128226.
- 36 Y. Zheng, Q. Zhou, Y. Yang, X. H. Chen, C. Wang, X. Zheng, L. Gao and C. L. Yang, *Small*, 2022, **18**, 2201223.
- 37 X. Y. Sun, H. Wei and B. Liu, *J. Phys. Chem. C*, 2022, **7**, 4753–4763.
- 38 B. Xu, Q. Hao, X. Tang and M. L. Chen, *Chem. Commun.*, 2023, **59**, 13474–13477.
- 39 Y. Zhu, S. C. Sun, H. Y. Li, L. Q. Kong, R. H. Xu, R. T. Fa, L. P. Wang and G. Li, *Eur. Polym. J.*, 2024, **202**, 112600.
- 40 X. Bao, W. Q. Sun, Z. Tian, H. Wang, X. D. Zhu, Z. X. Qian, H. Li and X. Yuan, *J. Mater. Chem. C*, 2024, **12**, 16774–16781.
- 41 Q. P. Zhang, S. H. Xu, L. P. Zhang, L. Yang and C. L. Jiang, *Adv. Sci.*, 2024, **11**, 2400781.
- 42 Y. C. Zhang, Q. H. Long, Y. J. Ding, C. Huang and M. M. Guo, *Carbon*, 2024, **217**, 118607.
- 43 Y. J. Ma, L. L. Wu, X. Y. Ren, Y. Q. Zhang and S. Y. Lu, *Adv. Funct. Mater.*, 2023, **33**, 2305867.
- 44 Y. Q. Zhang, M. Y. Li and S. Y. Lu, *Small*, 2023, **19**, 2606080.
- 45 X. Bao, X. D. Zhu, Z. Tian, H. Li, H. Li and Y. Diao, *J. Colloid Interface Sci.*, 2025, **690**, 137331.
- 46 L. Zhang, Y. Wang, Z. T. Bian, S. Komarneni and G. Z. Hang, *Opt. Mater.*, 2023, **145**, 114502.
- 47 X. L. Jin, H. Q. Zhao, H. Y. Bai, D. Liu and W. X. Chen, *Spectrochim. Acta, Part A*, 2024, **305**, 123473.
- 48 M. X. You, C. Li, Z. W. Zhang, Y. Zhang, W. Li, X. J. Zhang, J. L. Zhuang, C. F. Hu, H. W. Dong, Y. L. Liu, B. F. Lei and M. T. Zheng, *Chem. Eng. J.*, 2025, **505**, 159246.
- 49 S. Xu, R. F. Chen, C. Zheng and W. Huang, *Adv. Mater.*, 2016, **28**, 9920–9940.
- 50 Q. Lou, N. Chen, J. Y. Zhu, K. K. Liu, C. Li, Y. S. Zhu, W. Xu, X. Chen, Z. J. Song, C. H. Liang, C. X. Shan and J. H. Hu, *Adv. Mater.*, 2023, **21**, 2212286.
- 51 X. H. Shen, Y. J. Luo, K. Chen, C. Fu, R. Y. Liu, Y. Huang, K. Q. Wu, J. Luo and Z. Y. Lu, *Chem. Commun.*, 2023, **59**, 7036–7039.
- 52 Q. P. Zhang, S. H. Xu, L. P. Zhang, L. Yang and C. L. Jiang, *Adv. Sci.*, 2024, **11**, 2400781.
- 53 P. Zhang, L. Wang, H. Z. Guo, H. Li, S. Y. Wang, Y. L. Shan, T. Z. Chen, B. W. Chu, Q. X. Ma, Y. H. Wang, Y. B. Yu,

- M. H. Wu, J. S. Francisco and H. He, *J. Am. Chem. Soc.*, 2025, **147**(24), 20548–20558.
- 54 p. Liu, C. Liu, J. C. Chen and B. Wang, *Macromol. Mater. Eng.*, 2021, **306**, 2100339.
- 55 L. Ding, X. L. Jin, Y. C. Gao, S. W. Kang, H. Y. Bai, X. H. Ma, T. T. Ai, H. W. Zhou and W. X. Chen, *Nano Res.*, 2024, **17**, 5680–5687.
- 56 X. K. Xu, L. F. Cai, G. Q. Hu, L. Q. Mo, Y. H. Zheng and C. F. Hu, *J. Lumin.*, 2020, **227**, 117534.
- 57 Y. Q. Sun, J. K. Liu, X. L. Pang, X. J. Zhang, J. L. Zhuang, H. R. Zhang, C. F. Hu, M. Y. Zheng, B. F. Lei and Y. L. Liu, *J. Mater. Chem. C*, 2019, 1–7.
- 58 S. T. Luo, Y. J. Li, W. Yang, W. J. Gao, H. H. Yu and N. Huang, *ACS Appl. Mater. Interfaces*, 2023, **15**, 33848–33857.
- 59 H. C. Sun, P. F. Xia, H. B. Shao, R. Zhang, C. G. Lu, S. H. Xu and C. L. Wang, *J. Colloid Interface Sci.*, 2023, **646**, 932–939.
- 60 J. Wang and L. Chen, *Opt. Mater.*, 2024, **154**, 115749.
- 61 X. Y. Sun, M. T. Ouyang and X. Chen, *ACS Appl. Nano Mater.*, 2025, **8**, 5527–5534.
- 62 Z. M. Zhang, F. Vogelbacher, Y. L. Song, Y. Tian and M. Z. Li, *Exploration*, 2023, **3**, 20220052.
- 63 C. Y. Zheng, S. Y. Tao, X. X. Zhao, C. Y. Kang and B. Yang, *Angew. Chem., Int. Ed.*, 2024, **63**, e202408516.